Available online at www.sciencedirect.com
ScienceDirect
Journal of Power Sources 162 (2006) 696–705
JOURNAL OF POWER SOURCES
www.elsevier.com/locate/jpowsour

Effects of cell size and macrosegregation on the corrosion behavior of a dilute Pb–Sb alloy

Daniel M. Rosa, José E. Spinelli, Wislei R. Osório, Amauri Garcia *

Department of Materials Engineering, State University of Campinas–UNICAMP, P.O. Box 6122, 13083-970 Campinas, São Paulo, Brazil

Received 12 June 2006; received in revised form 6 July 2006; accepted 7 July 2006
Available online 14 August 2006

Abstract

The aim of this study was to examine the effect of cooling rate on the cellular growth of a Pb–0.85 wt%Sb alloy and to evaluate the influences of cell size and of the corresponding macrosegregation profile on the resultant corrosion behavior. In order to obtain the as-cast samples a water-cooled unidirectional solidification system was used. Such experimental set-up has permitted the development of a clear cellular structural array even for relative high cooling rates and has allowed a wide range of solidification conditions to be analyzed. Macrostructural and microstructural aspects along the casting were characterized by optical microscopy and scanning electron microscope (SEM) techniques. The electrochemical impedance spectroscopy technique and potentiodynamic curves (Tafel extrapolation) were used to analyze the corrosion resistance of samples collected along the casting length and immersed in a 0.5 M H_2SO_4 solution at 25 °C. It was found that the corrosion rate decreases with increasing cell spacing and that the pre-programming of microstructure cell size can be used as an alternative way to produce as-cast components of Pb–Sb alloys, such as battery grids, with better corrosion resistance.

Keywords: Pb–Sb alloy; Battery grids; Cellular microstructure; Macrosegregation; Corrosion resistance

1. Introduction

A battery grid must be dimensionally stable and have mechanical properties which can resist the stresses of the charge/discharge reactions without bending, stretching or warping. Additionally, the grid must not contain deleterious components that would hinder recycling [1]. The structural and mechanical characteristics of lead–antimony alloys as well as their precipitation hardening effect make them a very convenient material for lead-acid battery positive grids [2–5]. Such alloys are strong and creep-resistant and can be cast into rigid, dimensionally stable grids which are capable of resisting the stresses during operation [1,2]. It is also reported in the literature that the antimony content of a Pb–Sb electrode affects the mechanical properties, the microstructure, the electrochemical behavior of active materials and corrosion layers on the electrode (up to 3 wt%Sb is used for SLI battery grids) [4,6].

Solidification interface morphologies have been widely investigated by many metallurgists, physicists and mathematicians for several decades, in which cellular/dendritic growth is one of the most complicated solidification patterns and is also the most prevalent form of crystallization. The cellular and dendritic spacings are important microstructural parameters resulting from the solidification process, while it is well known that these spacings exercise a significant influence on the properties of castings. They affect the microscopic segregation existing between the cellular or dendritic ramifications. The growth of regular cells is favored by low growth rates and low level of solute content during solidification of alloys [7]. Some studies existing in literature have focused on the characterization of cellular and dendritic growth of Pb–Sb dilute alloys [8–11]. In a recent article, Rosa et al. [12] correlated solidification thermal variables with the cellular growth of dilute Pb–Sb alloys for transient unidirectional solidification.

It has been reported in the literature that the macrostructural and the microstructural as-cast morphologies affect the mechanical properties [13] and have also a strong influence on the corrosion resistance [14–17]. Recently, pure metals macrostructural [18] and binary aluminium alloy castings microstructural

* Corresponding author. Tel.: +55 19 37883320; fax: +55 19 32894217.
E-mail address: amaurig@fem.unicamp.br (A. Garcia).

0378-7753/$ – see front matter © 2006 Elsevier B.V. All rights reserved.
doi:10.1016/j.jpowsour.2006.07.016

[19–21] effects upon the tendency of corrosion resistance have been reported. It was found that the tendency of improvement on the corrosion resistance depends on the cooling rate imposed during solidification which affects dendrite arm size and solute redistribution, and on the electrochemical behavior of solute and solvent.

Studies of lead–antimony alloys assessing the influences of both the microstructural morphology and of solute redistribution on surface corrosion resistance are very scarce in the literature. Rezaei and Damiri [4] concluded in a recent research that the control of cooling rate is very important for the grid casting process in order to get better electrochemical behavior, which strongly affects grid performance. They observed that lower cooling rates imposed during solidification of a lead–antimony alloy casting provide antimony segregation to the interior of the casting, while surface antimony concentrations significantly decrease.

The aim of this study was to examine the effect of cooling rate on the cellular growth of a dilute Pb–Sb alloy and to evaluate the influences of cell size and of the corresponding macrosegregation profile on the resultant corrosion behavior. For this purpose, a Pb–0.85 wt%Sb alloy and a water-cooled unidirectional solidification system were used. Such experimental set-up has permitted the development of a clear cellular array even for relative high cooling rates and has allowed a wide range of solidification conditions to be analyzed. Corrosion tests were performed with samples of different cell sizes in a 0.5 M H_2SO_4 solution at 25 °C, and the corrosion rate was correlated with both the cellular spacing and the Sb segregation profile.

2. Experimental procedure

A Pb–0.85 wt%Sb alloy, which was prepared from commercially pure metals, with chemical compositions shown in Table 1, was used in the experiments.

The solidification set-up is detailed in Fig. 1. It was designed in such way that the heat was extracted only through the water-cooled bottom, promoting vertical upward directional solidification. The stainless steel mold had an internal diameter of 50 mm, height 110 mm and a 3 mm wall thickness. The side walls were covered with a layer of insulating alumina to minimize radial heat losses. The bottom part of the mold was closed with a thin (3 mm thick) stainless steel sheet, which physically separates the metal from the cooling fluid.

Table 1
Chemical composition of metals used to prepare the Pb–Sb alloy

Metal	Chemical composition (wt%)					
	Fe	Si	Na	Cu	Pb	S
Sb	0.053	0.017	0.298	0.030	0.247	0.022
Pb	0.051	0.080	*	*	*	*

* Less than 50 ppm.

The alloy was melted in situ and the lateral electric heaters had their power controlled in order to permit a desired melt superheat to be achieved. To start solidification, the electric heaters were disconnected and at the same time the controlled water flow was initiated. The thermal acquisition system, which is composed of a data logger and a data reading software, was run from the signals of type J thermocouples. All thermocouples were calibrated considering the melting temperature of lead, exhibiting fluctuations of about 0.4 °C. Six thermocouples, sheathed in 1.6 mm outside diameter stainless steel protection tubes, were placed close to the central part of the cylindrical ingot and temperature was monitored during solidification at 5, 10, 15, 30, 50 and 70 mm from the heat extracting surface. The thermal readings were collected through an acquisition rate of two measurements per second.

The cylindrical ingot was sectioned on a midplane, grinded, polished and etched with a solution to reveal the macrostructure. Transverse sections (perpendicular to the growth direction) from the directionally solidified specimen at six different positions along the ingot length were polished and etched with a solution (37.5 mL of glacial acetic acid and 15 mL of H_2O_2, at 25 °C) for microscopy examination. Image processing systems Neophot 32 (Carl Zeiss, Esslingen, Germany) and Leica Quantimet 500 MC (Leica Imaging Systems Ltd., Cambridge, England) were used to measure the cellular spacings (λ_1). The method used for measuring λ_1 on the transverse section of each sample was the triangle method [6]. Forty λ_1 values were measured for each

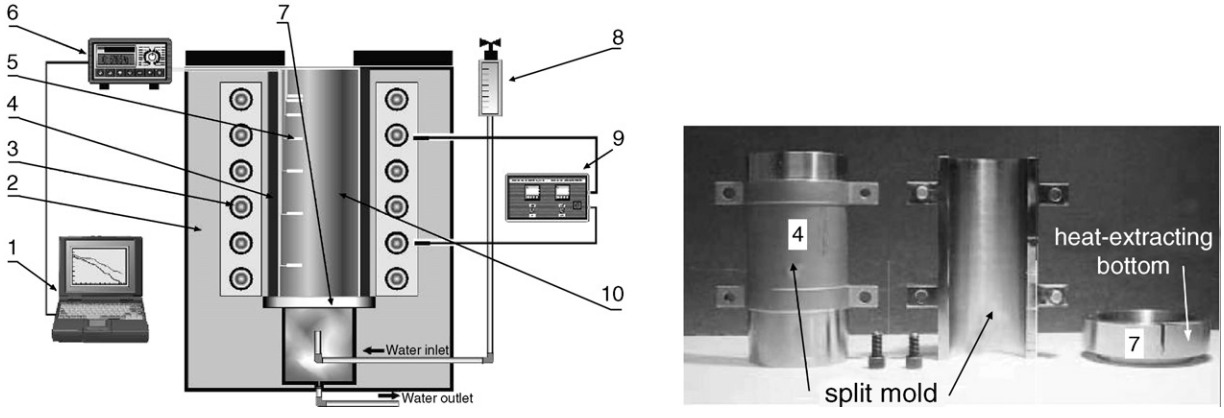

Fig. 1. Schematic representation of the experimental solidification set-up: (1) computer and data acquisition software; (2) insulating ceramic shielding; (3) electric heaters; (4) mold; (5) thermocouples; (6) data logger; (7) heat-extracting bottom; (8) water flow meter; (9) temperature controller; (10) casting.

selected position from the casting bottom. The macrosegregation profile was determined by a scanning electron microscope (SEM, JMS T20 of Jeol Co., Japan) and an energy dispersive X-ray analyzer (EDAX, NORAN, System Six 1.5, USA).

In order to establish correlations between the corrosion resistance and the microstructural pattern, electrochemical impedance spectroscopy (EIS) and polarization tests were carried out on samples collected at different positions along the casting length. The EIS tests were carried out in a 500 mL of sulfuric acid solution (0.5 mol L^{-1}) at 25 °C. A potentiostat coupled to a frequency analyzer system, a glass corrosion cell kit with a platinum counter electrode and a saturated calomel reference electrode (SCE) were used. The working electrodes consisted of casting alloy samples which were positioned at the glass corrosion cell kit, leaving a circular 1 cm^2 metal surface in contact with the electrolyte. The potential amplitude was set to 10 mV in open-circuit potential and the frequency range was set from 100 mHz to 100 kHz. The samples were further ground to a 600 grit SiC finish, followed by distilled water washing and air drying before measurements. EIS measurements began after an initial delay of 30 min for the sample to reach a steady-state condition.

Polarization tests were also carried out in a 500 mL of sulfuric acid solution (0.5 mol L^{-1}) at 25 °C using an EG&G Princeton Applied Research, model 273A potentiostat. Such potentiodynamic polarization curves were determined at a scan rate of 0.2 mV s^{-1} from −250 mV (SCE) to +250 mV (SCE) related to open-circuit potential. Using an automatic data acquisition system, the potentiodynamic polarization curves were plotted and both corrosion rate and potential were estimated by the Tafel extrapolation method [22].

3. Results and discussion

The experimental thermal analysis along the casting resulted in six typical cooling curves which are representative of solidification evolution along the casting length (Fig. 2).

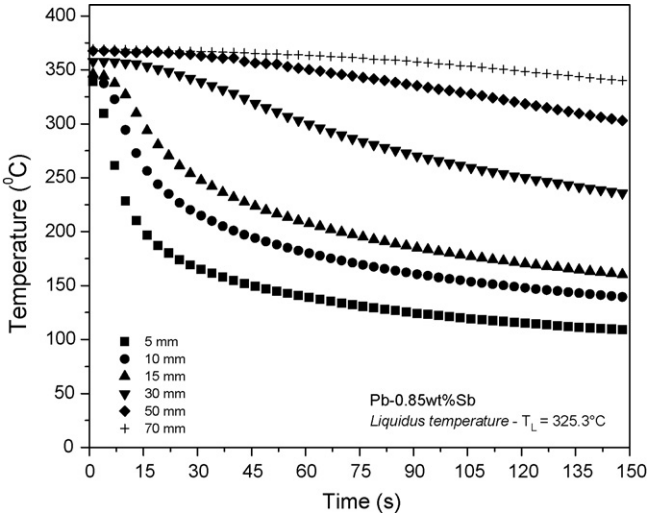

Fig. 2. Experimental cooling curves for a Pb–0.85 wt%Sb alloy during vertical directional solidification.

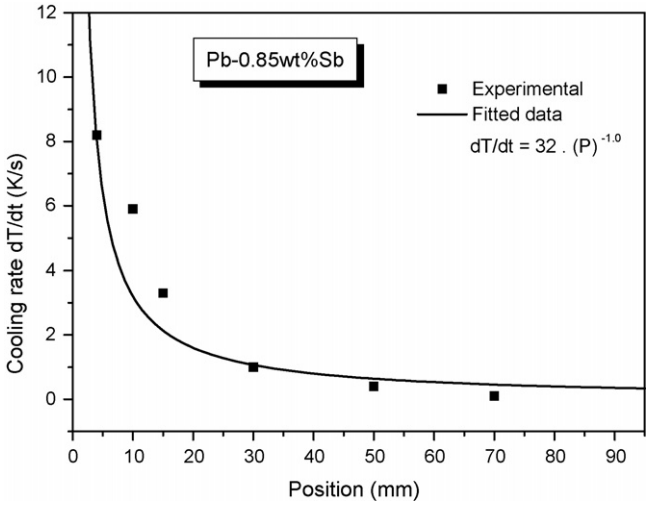

Fig. 3. Cooling rate as a function of position (P) from the casting/chill surface.

The data acquisition system employed during the experiment has permitted accurate determination of the slope of the experimental cooling curves. Hence, the tip cooling rate was determined by considering the thermal data recorded immediately after the passing of the liquidus front by each thermocouple. Fig. 3 shows the experimentally determined cooling rates along the casting. It can be observed that a considerable range of cooling rate values was generated as a result of the high efficiency

Fig. 4. Directionally solidified macrostructure of a Pb–0.85 wt%Sb alloy casting.

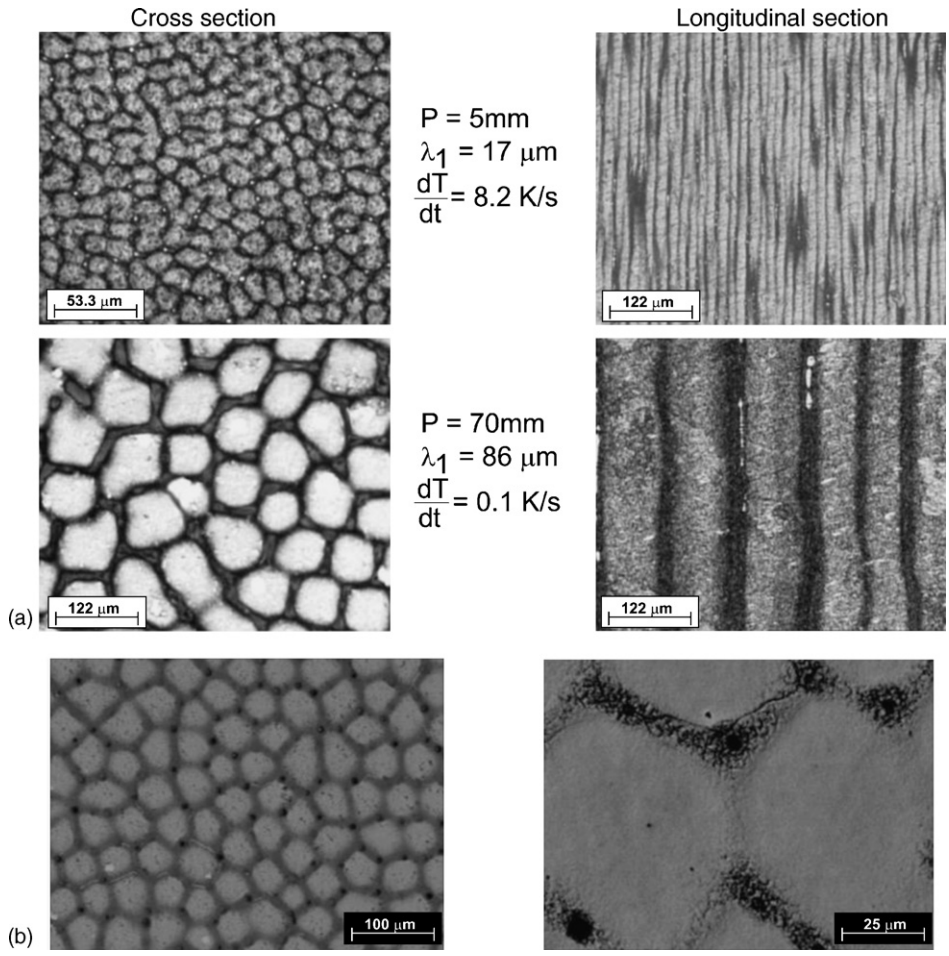

Fig. 5. Typical microstructures of the Pb–0.85 wt%Sb alloy. (a) Optical microscopy images at 5 and 70 mm from the casting/chill surface and (b) SEM images at 30 mm (cross-section).

of the imposed heat extraction, especially at the first stages of solidification.

Fig. 4 shows the resultant directionally solidified casting macrostructure. It can be seen that the growth of columnar grains prevailed along the entire casting length. The typical microstructures observed on both transverse and longitudinal sections of the Pb–0.85 wt%Sb alloy casting are shown in Fig. 5. The final structure immediately after solidification consists of a cellular array formed by a Pb-rich matrix (α-phase: solid solution of Sb in Pb) with a eutectic mixture in the intercellular regions constituted of α, and a Sb-rich β-phase (solid solution of Pb in Sb).

The experimental evolution of cellular spacings (λ_1) as a function of position from the casting/chill surface is shown in Fig. 6(a). Points are experimental results and the line represents an empirical power function fit to the experimental points. Minimum and maximum measured λ_1 values for each position are expressed by the error bars. The positions along the casting from where the samples for corrosion tests were collected are shown in Fig. 6(b).

The experimental cooling rate dependence on cellular spacing is shown in Fig. 7, where average spacings along with the standard variation are presented. The line represents an empirical power law which fits the experimental points.

It can be seen in Fig. 3 that the use of a water-cooled mold imposes higher values of tip cooling rates near the casting/chill surface and a decreasing profile along the casting length due to the increase of the thermal resistance of the solidified shell with distance from the cooled surface. This influence translates to the observed experimental values of cellular spacings, with fine cells close to the casting cooled surface and coarser ones far from it. As can be observed in Fig. 5(a), the number of aligned cells in a same area of analysis is remarkably distinct at longitudinal microstructures close to (5 mm) and far from (70 mm) the casting cooled surface.

Electrochemical analyses with potentiodynamic polarization curves related to open-circuit have been carried out with pure Pb and Sb samples. The resulting mean values of open-circuit corrosion potentials were −553 mV (versus SCE) and −345 mV (versus SCE) for lead and antimony, respectively. This is an indication of a nobler corrosion behavior of antimony, which is in agreement with a recent study of electrochemical characteristics of Pb–Sb alloys in sulfuric acid solutions [2].

Figs. 8(a and b) show experimental EIS results in Bode and Bode-phase representation, respectively, for Pb–0.85 wt%Sb alloy samples collected at different positions along the casting length. It can be seen that both the modulus of impedance and the phase angle (both represented as a function of frequency)

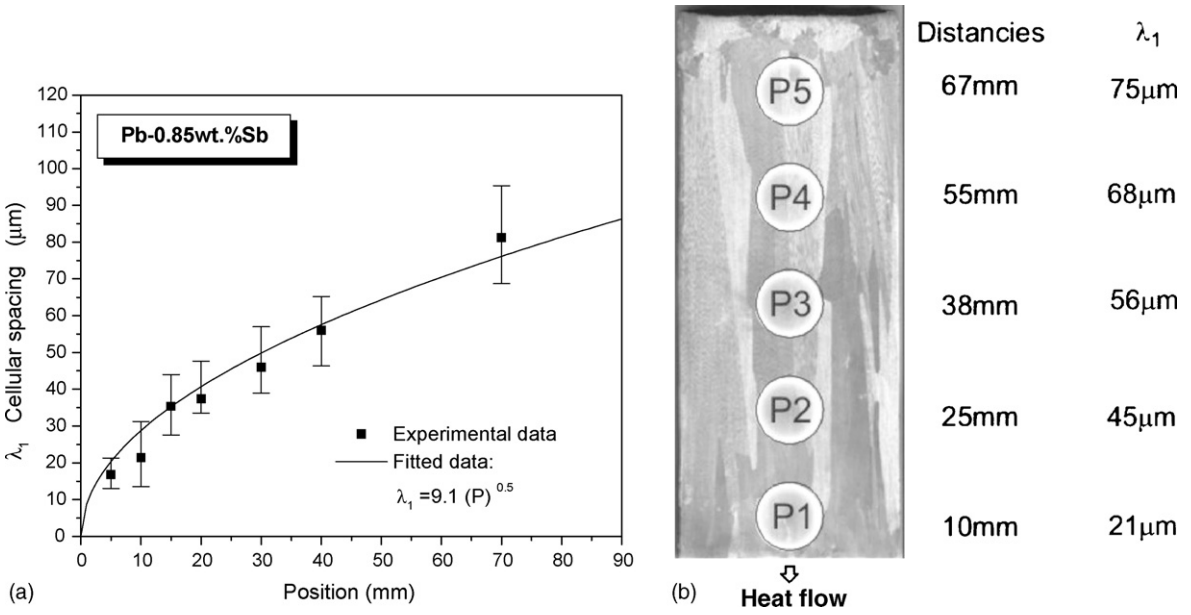

Fig. 6. (a) Cellular spacing as a function of position from casting/chill surface and (b) positions from where samples were collected for corrosion tests and the corresponding mean values of cell spacing.

increase with increasing distance from the casting/chill surface for the three first positions which are closer to the casting bottom (P1–P3). As a direct consequence, both impedance and phase values increase with increasing cellular spacings. It is well known that higher impedance and phase angle are conducive to nobler electrochemical behavior. In contrast, positions P4 and P5 (closer to the top of the casting) are associated with lower values of impedance and phase angle when compared with those of the positions P1–P3. This seems to be associated with the solute (Sb) redistribution along the casting length during the solidification process. The corresponding macrosegregation profile, shown in Fig. 9, demonstrates that positions closer to the casting top have antimony contents higher than the alloy nominal composition, while positions closer to the casting surface have concentrations lower than 0.85 wt%Sb. It can be seen that the Sb concentrations at positions P1, P2 and P3 are quite close, while positions P4 and P5 have higher antimony contents. The macrosegregation

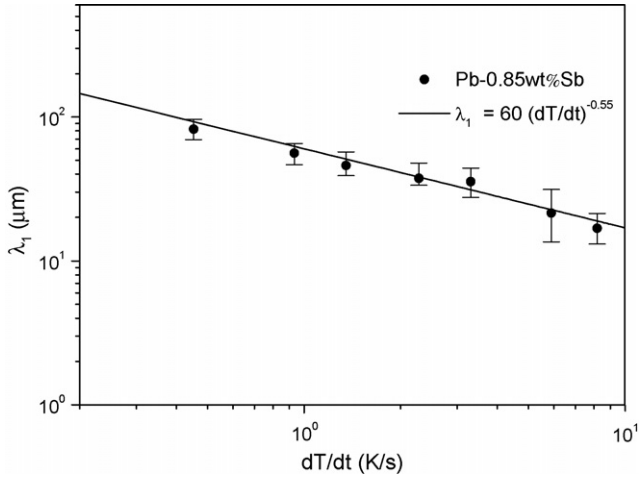

Fig. 7. Cellular spacings as a function of cooling rate.

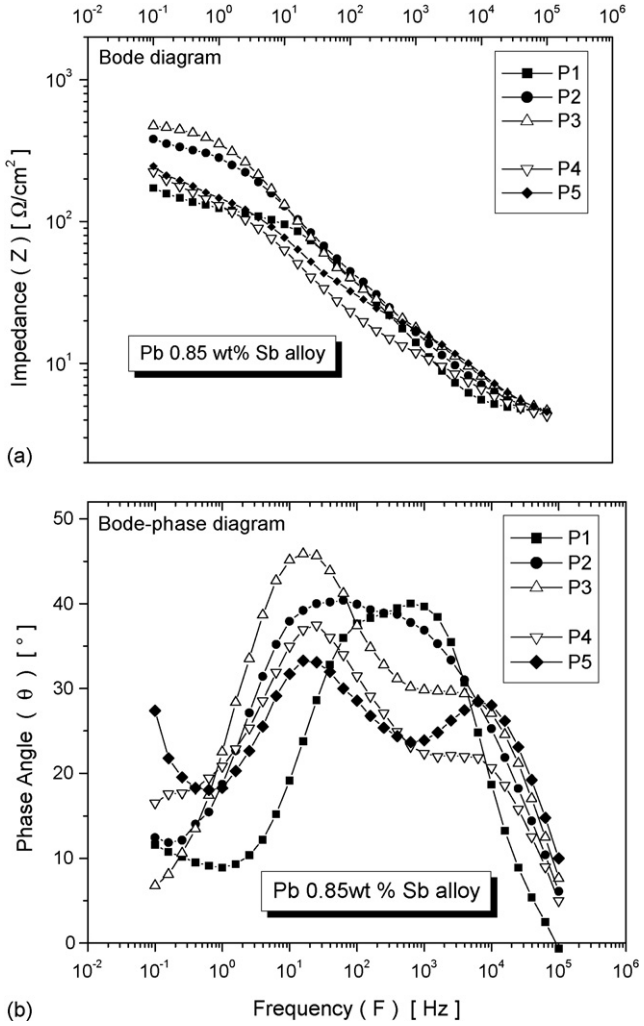

Fig. 8. Results of EIS tests in: (a) Bode and (b) Bode-phase representation.

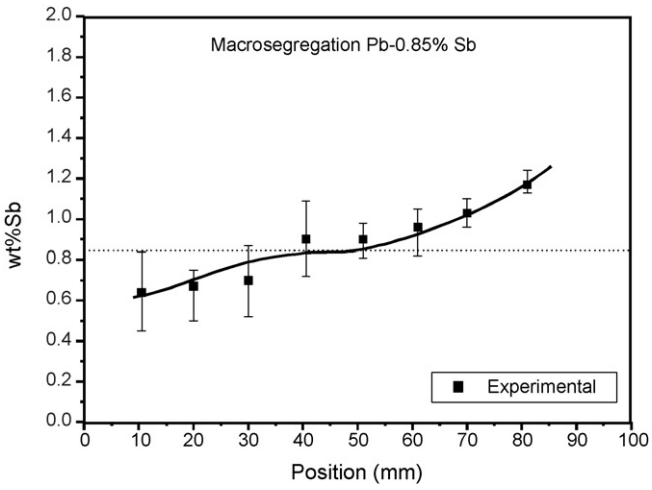

Fig. 9. Macrosegregation profile along the casting length.

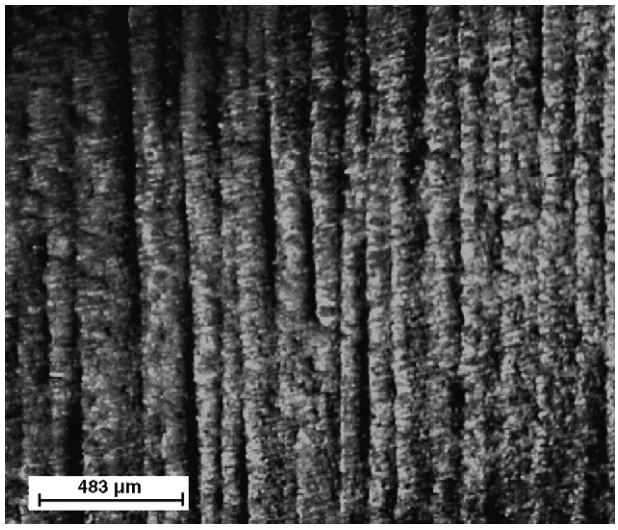

Fig. 10. Optical image of a Pb–0.85 wt%Sb sample collected at position P5 (longitudinal section) and etched in 80% sulfuric acid.

profile has the typical trend of a normal segregation distribution for a solute redistribution coefficient less than unity. It can also be slightly affected by solution convection, since the solute profile inside the mushy zone and in the overlying melt ahead of the cellular tips is expected to be unstable because the solute enrichment decreases the melt density.

It can be observed in Fig. 6 that the corresponding mean value of the measured cell spacing for position P1 is remarkably lower than those corresponding to the other positions (P2–P5). Fine cell spacings are associated with an increase in cell boundaries. These boundaries are regions of higher energy which is a result of distortions at the limits between adjacent cells during growth along the solidification process. The resulting corrosion behavior seems to be similar to that observed for pure metals with fine and large equiaxed grains. Larger grains structures have proved to be more corrosion resistant. In this case, the grain boundaries are regions of preferable corrosion action as a result of the residual stresses caused by plastic deformation at the boundaries during growth [19,23]. Furthermore, slight lower antimony content is observed at position P1. This particular metallurgical condition seems to influence the corrosion kinetics, as position P1 presents only one time constant while the other four positions exhibit two time constants. In the case of positions P2–P5, two different corrosion mechanisms may be expected: high frequency (of about 10^3 Hz) corresponding to the dissolution of the Pb-rich matrix and low frequency (of about 10^1 Hz) referring to the corrosion in the intercellular region. It can also be observed in Fig. 8(a) that the kinetics of the double layer formation at positions P4 and P5 is slightly different when compared to that of positions P1, P2 and P3, which are quite similar.

In order to assess the corrosion action from the cell center to the boundary, a sample collected at position P5 has been subjected to an etching test in an 80 vol% of H_2SO_4 solution for 60 s, and immediately after etched observed at the optical microscope. The resulting image is shown in Fig. 10, where it can be clearly seen that the cells boundaries are more deeply corroded than the cells cores.

In order to supply quantitative support for discussions of these experimental EIS results, an appropriate model (ZView Version 2.1b) for equivalent circuit quantification has also been used. Fig. 11 shows the equivalent circuit chosen to fit the experimental data. The examples of experimental and simulated agreement for positions P1 and P3 indicate that the experimental results are well fitted to the proposed equivalent circuit. This equivalent circuit is similar to that proposed by Mansfeld and Kendig to represent the oxide layer of anodized aluminium [24]. It has also been used by other researchers to represent different oxide layer formations [25,26]. The fitting quality was evaluated by chi-square (χ^2) values of about 10^{-3}, which were interpreted by the ZView software.

According to a report from the literature, the oxide layer formed at the surface of an alloy consists of a barrier-like inner layer and a porous outer layer [26]. Concerning the processes taking place on the working electrode surface, it is important to remark that the solubility of $PbSO_4$ in 0.5 M H_2SO_4 is relatively high, and only small amounts of $PbSO_4$ crystals will be formed and reduced (dissolution–precipitation mechanism). There are no conditions for the formation of a $PbSO_4$ semi-permeable porous membrane layer. Due to the low potential values, a PbO resistive layer will not be formed. Sb(III) and Sb(V) ions will be also not formed. A similar situation with the potentiodynamic sweeps is expected [27].

The physical significance of the circuit elements is the following [28]. $Z_{CPE(1)}$ denotes the double layer capacitance, R_{el} the electrolyte resistance which in Bode plot are expressed in a high frequency limit ($F > 1$ kHz), R_1 the charge transfer resistance, and $Z_{CPE(2)}$ and R_2 stand for a capacitance and a resistance due to the participation of adsorbed intermediates. The parameters n_1 and n_2 are correlated with the phase angle, varying between -1 and 1. In the literature, Z_{CPE} generally denotes the impedance of a phase element as $Z_{CPE} = [C(jw)^n]^{-1}$ [29,30]. However, in the present investigation, for the mathematical analysis of impedance diagrams, a constant phase element, CPE, was used instead of an "ideal" capacitor and $Z_{CPE(1)}$ and $Z_{CPE(2)}$ are defined as capacitances. The impedance parameters are shown in Table 2.

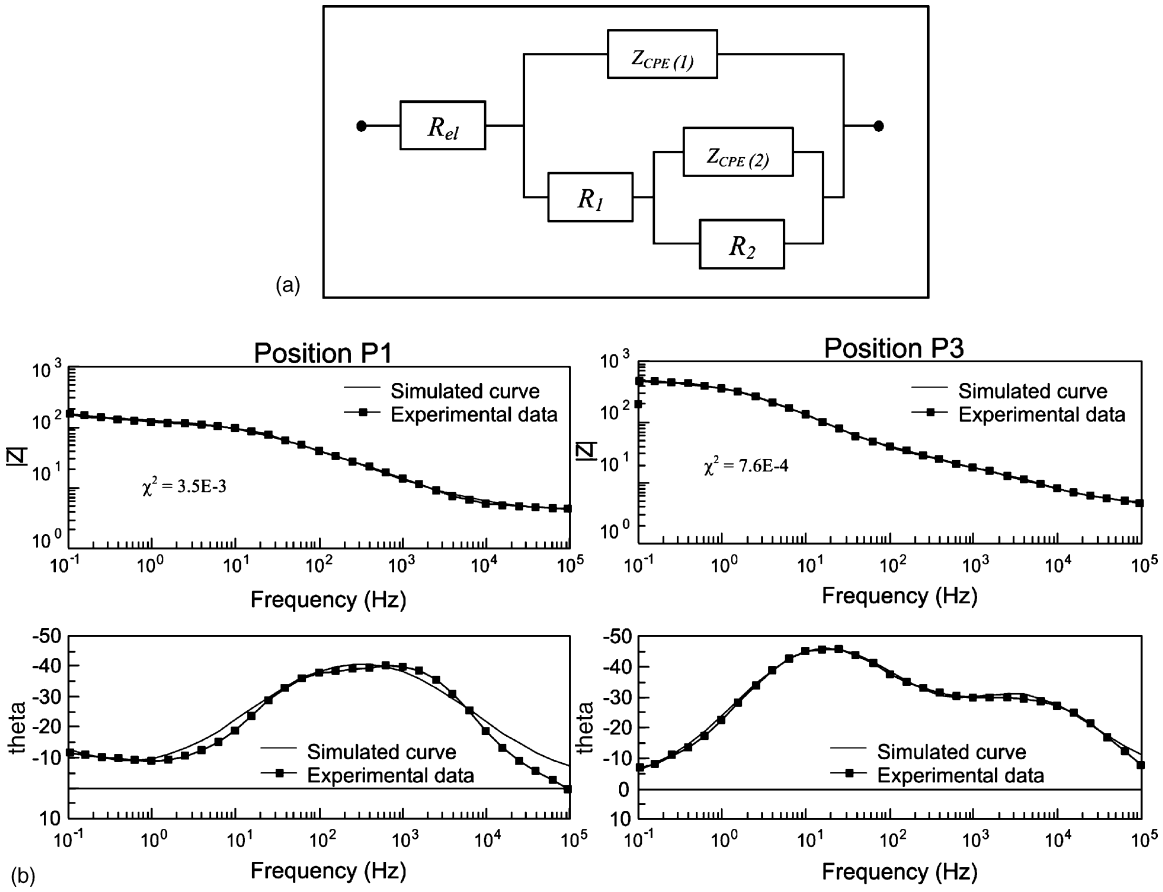

Fig. 11. (a) Equivalent circuit for modeling impedance data performed in a 0.5 M of H_2SO_4 solution and (b) experimental data and simulated curves by using the ZView software.

In Bode-phase plots (Fig. 8(b)), it can be observed that position P1 is associated with one time constant, as discussed previously, and values of R_1 and R_2 for P1 are very close, as shown in Table 2. In contrast from P2 to P5, R_2 values are significantly higher than R_1. This fact could suggest that R_2 is the main factor providing protection or increasing the tendency of corrosion resistance along the casting length. Assis et al. [26] have observed a similar effect on Ti–Al alloys.

By analyzing the parameters in Table 2, it can be seen that positions P1–P3 have higher capacitances $Z_{CPE(1)}$ and polarization resistances R_1 if compared with those associated with positions closer to the ingot top (P4–P5). This seems to be caused by: (i) poorer concentration of antimony at regions closer to the casting bottom (Fig. 9), since Sb is electrochemically nobler than Pb and (ii) as shown by the microstructures (Fig. 5), casting top regions have thicker cells than regions which are closer to the casting/chill surface. The corrosion action was shown to be stronger at the cell boundaries, and as a result finer cell regions will be subjected to more generalized corrosion due to the more extensive boundaries distribution, which are typical of these refined regions. It can be seen in Table 2 that positions P2 and P3 have similar impedance parameters ($Z_{CPE(1\text{ and }2)}$ and R_1 and R_2). Likewise, an analysis concerning P4 and P5 resulted in similar values of every determined parameter. Thus, a direct comparison between P2/P3 and P4/P5 can be accomplished. For example, $Z_{CPE(1)}$ for P2/P3 is represented by the range 135–117 $\times 10^6/\Omega^{-1}\,s^n\,cm^{-2}$ (or 135–117 $\mu F\,cm^{-2}$),

Table 2
Impedance parameters for a Pb–0.85 wt%Sb alloy in a 0.5 M of H_2SO_4 solution

Parameters	P1*	P2*	P3*	P4*	P5*
R_{el} ($\Omega\,cm^{-2}$)	3.98	4.20	4.18	4.28	4.54
$Z_{CPE(1)}$ ($10^6/\Omega^{-1}\,s^n\,cm^{-2}$)	426.53 ± 32.3	135.69 ± 5.3	117.39 ± 4.3	7.46 ± 4.1	9.40 ± 7.1
$Z_{CPE(2)}$ ($10^3/\Omega^{-1}\,s^n\,cm^{-2}$)	33.00 ± 5.3	0.48 ± 0.36	0.27 ± 0.18	1.72 ± 0.96	1.48 ± 4.1
n_1	0.61	0.68	0.67	0.93	0.88
n_2	0.82	0.56	0.73	0.54	0.53
R_1 ($\Omega\,cm^{-2}$)	139	25.5	26.4	4.73	9.90
R_2 ($\Omega\,cm^{-2}$)	120	388	467	250	265

* Positions from the casting/chill surface corresponding to Fig. 6(b).

which is one order of magnitude higher than $Z_{CPE(1)}$ for P4/P5 (7.46–9.40 μF cm^{-2}).

The impedance parameters obtained for position P1 confirm the discussions based on Fig. 8(b), i.e., position P1 has a different corrosion behavior due to the smaller cell spacing associated to the lower antimony content. It presents only one time constant while the other four positions exhibit two. EIS diagrams and impedance parameters permit to conclude that the tendency of corrosion resistance increases with increasing cellular spacing.

Fig. 12 shows experimental potentiodynamic polarization curves for different positions along the casting length. The corrosion current densities (i_{Corr}) were obtained from the polarization curves by Tafel plots using both cathodic and anodic branches of the polarization curves. The resulting average current densities and their correspondent corrosion potentials are shown in Fig. 12. Such results permit to reinforce the corrosion resistance tendency which has been observed when analyzing both EIS diagrams and the equivalent circuit results. The corrosion current density (corrosion rate) at position P1 is higher than those of subsequent positions, as shown in Fig. 12, i.e., the corrosion resistance increases with increasing distance from the casting cooled surface.

The present experimental results have shown that coarser cells tend to improve the corrosion resistance of a Pb–0.85 wt%Sb alloy mainly due to the reduction of cellular boundaries. This condition provides a better galvanic protection when compared to the microstructure of the initial positions,

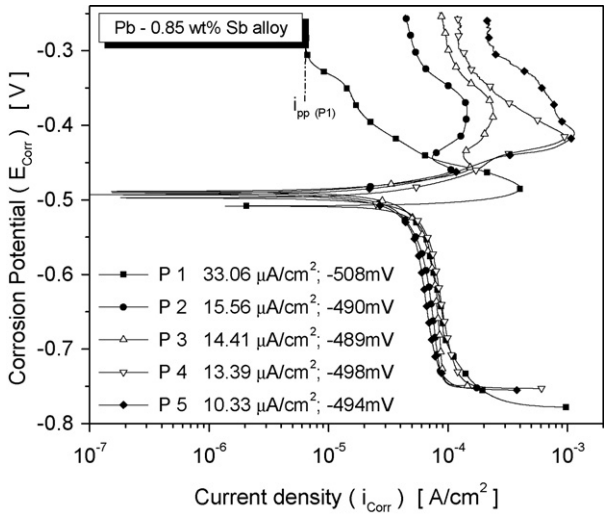

Fig. 12. Experimental potentiodynamic polarization curves for a Pb–0.85 wt%Sb alloy in 0.5 M of H_2SO_4 solution at 25 °C.

which is characterized by finer cellular spacings. Fig. 13 shows a schematic representation of fine and coarse cellular structures emphasizing the proposed mechanism, which is dependent on the distribution of intercellular regions. A finer cellular microstructure is characterized by several parallel boundaries. In this sense, smaller cell spacings will induce a more extensive corrosion action, being more susceptible to galvanic degrada-

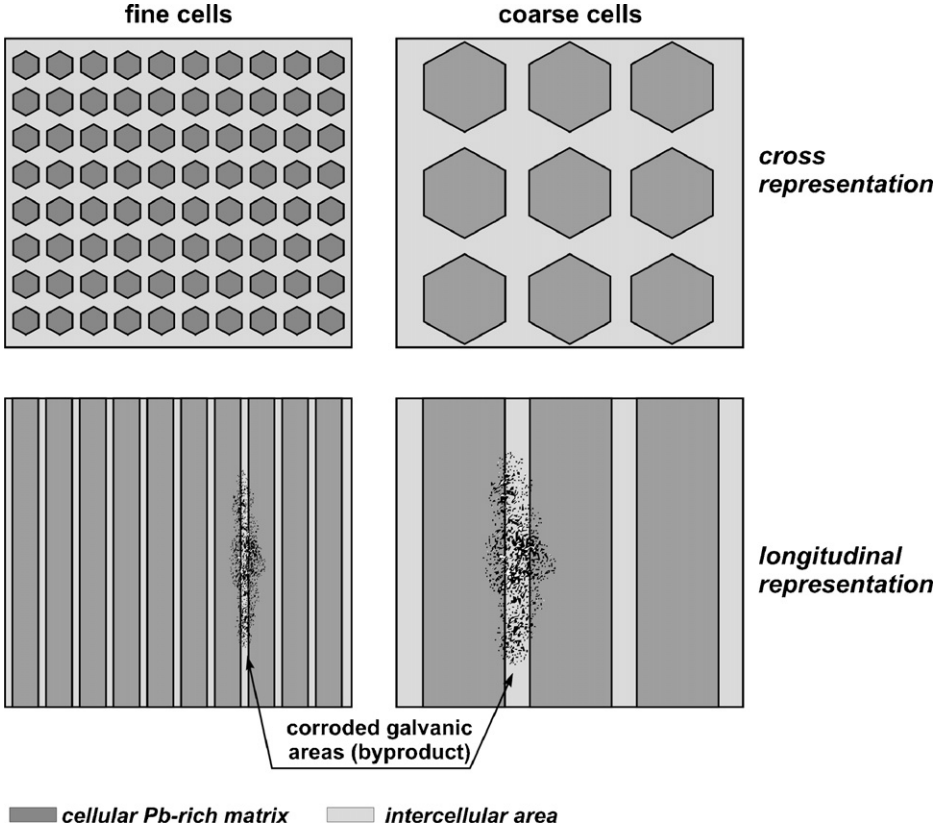

Fig. 13. Schematic representation of fine and coarse cellular morphologies and their different galvanic protection due to cell size.

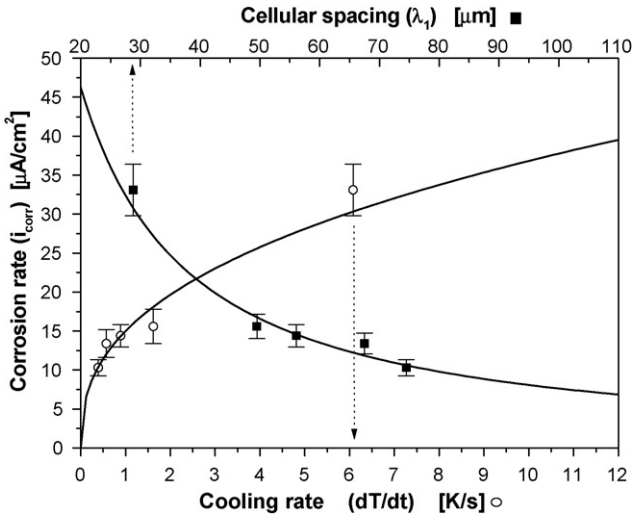

Fig. 14. Experimental corrosion rates of Pb–0.85 wt%Sb alloy samples as a function of cellular spacing and of cooling rate.

tion. On the other hand, microstructures characterized by coarser cells present less boundaries and preserved areas at the cell core should be expected.

Although the potentiodynamic polarization curves have provided sufficient information about the tendency of corrosion resistance of a Pb–0.85 wt%Sb alloy in sulfuric acid solution in terms of corrosion rate, the passivity behavior can also be observed through this analysis, since it is well known that the passivity phenomenon can occur to lead alloys when immersed in sulfuric acid.

Fig. 14 shows the corrosion rate as a function of both cellular spacing (solid squares) and cooling rate during solidification (open circles). It can be seen that the corrosion rate decreases with increasing cell size. In contrast, the cell size is imposed by the cooling rate during solidification, which is a thermal variable that depends on the operational conditions of the casting system. It can be seen in Fig. 14 that a corrosion rate of about 30 $\mu A\,cm^{-2}$, corresponds to values of cooling rate and cellular spacing of about 6 $K\,s^{-1}$ and 28 μm, respectively. On the other hand, a corrosion rate of about 10 $\mu A\,cm^{-2}$ can be related to a cooling rate and a cellular spacing of 0.4 $K\,s^{-1}$ and 75 μm, respectively. The results provided in Fig. 14 can be used in the control of as-cast cellular microstructures of Pb–Sb alloys by manipulating the solidification processing variables. The preprogramming of the microstructure cell size can be used as an alternative way to produce components, such as battery grids, with better corrosion resistance.

4. Conclusions

The following main conclusions can be drawn from the present experimental investigation:

1. The experimental EIS diagrams, potentiodynamic polarization curves and fitted equivalent circuit parameters have shown that coarser cellular structures tend to yield higher corrosion resistance than finer cellular structures for a Pb–0.85 wt%Sb alloy. Such tendency of better corrosion resistance presented by coarser cells seems to be associated with the reduction of cellular boundaries when compared with finer cells, since the boundary has proved to be more susceptible to the corrosion action.
2. The control of as-cast cellular microstructures, by manipulating solidification processing variables permitting the control of cooling rate, can be used as an alternative way to produce as-cast components of Pb–Sb alloys, such as battery grids, with better corrosion resistance.

Acknowledgements

The authors acknowledge financial support provided by FAPESP (The Scientific Research Foundation of the State of São Paulo, Brazil), FAEPEX-UNICAMP and CNPq (The Brazilian Research Council).

References

[1] R.D. Prengaman, J. Power Sources 67 (1997) 267–278.
[2] T. Hirasawa, K. Sasaki, M. Taguchi, H. Kaneko, J. Power Sources 85 (2000) 44–48.
[3] G.S. Al-Ganainy, M.T. Mostafa, F. Abd El-Salam, Phys. B 348 (2004) 242–248.
[4] B. Rezaei, S. Damiri, J. Solid State Electrochem. 9 (2005) 590–594.
[5] M. Shiota, T. Kameda, K. Matsui, N. Hirai, T. Tanaka, J. Power Sources 144 (2005) 358–364.
[6] R.D. Prengaman, J. Power Sources 95 (2001) 224–233.
[7] O.L. Rocha, C.A. Siqueira, A. Garcia, Mater. Sci. Eng. A 361 (2003) 111–118.
[8] L. Yu, G.L. Ding, J. Reye, S.N. Ojha, S.N. Tewari, Metall. Mater. Trans. A 30A (1999) 2463–2471.
[9] S.P. O'Dell, G.L. Ding, S.N. Tewari, Metall. Mater. Trans. A 30A (1999) 2159–2165.
[10] J. Hui, R. Tiwari, X. Wu, S.N. Tewari, R. Trivedi, Metall. Mater. Trans. A 33A (2002) 3499–3510.
[11] J. Chen, S.N. Tewari, G. Magadi, H.C. de Groh III, Metall. Mater. Trans. A 34A (2003) 2985–2990.
[12] D.M. Rosa, J.E. Spinelli, I.L. Ferreira, A. Garcia, J. Alloys Compd., in press, available online.
[13] P.R. Goulart, J.E. Spinelli, W.R. Osório, A. Garcia, Mater. Sci. Eng. A 421 (2006) 245–253.
[14] K.G. Watkins, M.A. McMahon, W.M. Steen, Mater. Sci. Eng. A 231 (1997) 55–61.
[15] I. Garcia, J.J. de Damborenea, Corros. Sci. 40 (1998) 1411–1419.
[16] G. Song, A. Atrens, M. Dareusch, Corros. Sci. 41 (1999) 249–273.
[17] G. Song, A.L. Bowles, D.H. StJohn, Mater. Sci. Eng. A 366 (2004) 74–86.
[18] W.R. Osório, C.M.A. Freire, A. Garcia, Mater. Sci. Eng. A 402 (2005) 22–32.
[19] W.R. Osório, C.M.A. Freire, A. Garcia, J. Alloys Compd. 397 (2005) 179–191.
[20] W.R. Osório, C.M.A. Freire, A. Garcia, J. Mater. Sci. 40 (17) (2005) 4493–4499.
[21] W.R. Osório, J.E. Spinelli, N. Cheung, A. Garcia, Mater. Sci. Eng. A 420 (2006) 179–186.
[22] M. Stern, A.L. Geary, J. Electrochem. Soc. 4 (1957) 56–63.
[23] W.R. Osório, C.A. Siqueira, C.M.A. Freire, A. Garcia, Rev. Metal. Madrid Extr. (2005) 176–180.
[24] F. Mansfeld, M.W. Kendig, J. Electrochem. Soc. 135 (1988) 828–835.

[25] J. Pan, D. Thierry, C. Leygraf, Electrochim. Acta 41 (1996) 1143–1153.
[26] S.L. de Assis, S. Wolynec, I. Costa, Electrochim. Acta 51 (2006) 1815–1819.
[27] D. Pavlov, M. Bojinov, T. Laitinen, G. Sundholm, Electrochim. Acta 36 (1991) 2087–2092.
[28] D. Pavlov, M. Bojinov, T. Laitinen, G. Sundholm, Electrochim. Acta 36 (1991) 2081–2086.
[29] M. Kliskic, J. Radosevic, S. Gudic, M. Smith, Electrochim. Acta 43 (1998) 3241–3255.
[30] S. Gudic, J. Radosevic, M. Kliskic, Electrochim. Acta 47 (2002) 3009–3016.